Thermal diffusivity measurements in a sheared particle-laden suspension

A. P. Merin and Vinod Srinivasan*
Mechanical Engineering, University of Minnesota–Twin Cities, Minneapolis, Minnesota 55455, USA

(Received 9 March 2026; accepted 31 July 2026; published 8 September 2026)

This study examines the effective thermal diffusivity of sheared particle-fluid suspensions with non-Brownian neutrally buoyant particles in a thin gap Taylor-Couette cell. A steady canonical shear flow is generated with Taylor instabilities suppressed by outer cylinder rotation. Spherical acrylic particles of 1.93 mm diameter were used with a density-matched propylene glycol-glycerol solution. Thermal diffusivity of the medium is deduced by applying a thermal pulse to the stationary inner cylinder and monitoring temporal temperature decay on the inner cylinder surface. The study documents the effects of the particle Peclet number ($<$1400) for four different particle volume fractions of 0.14, 0.22, 0.30, and 0.36. Here the Peclet number is defined as the ratio of timescales of thermal diffusion in the liquid over the particle scale to the timescale of the imposed shear. The applied shear corresponded to particle Reynolds numbers ranging from Stokes flow ($\mathrm{Re}_p \ll 1$) to a maximum of 0.85, where weak inertial effects are likely present. At low Peclet number $\mathrm{Pe} < 100$, the enhancement due to shear is roughly linear with the Peclet number. At higher Pe ($100 < \mathrm{Pe} < 700$), the enhancement displays power-law behavior with an exponent of 1/2, which has been predicted by some models for concentrated suspensions, but is also consistent with the emergence of a particle-free fluid layer near one wall. At still higher Pe, the 1/2 power-law behavior is retained for all but the highest volume fractions, with $\phi = 0.35$ exhibiting a 1/11 power-law behavior, which has been previously predicted, albeit for dilute suspensions, for the high-Pe limit. The thermal diffusivity measurements are complemented by limited measurements of particle velocity through particle tracking, which suggest that particle motion does not contribute significantly to the observed enhancement at high Peclet numbers.

DOI: 10.1103/7b71-gckp

I. INTRODUCTION

Heat transport in dense suspensions is important in many engineering applications, such as concrete mixing [1], coal combustion [2], fluidized bed reactors [3,4], and the preparation of foods and cosmetics. Natural systems where scalar transport is influenced by the presence of particles in a fluid include pyroclastic lava flows [5] and nutrient transport alongside erythrocytes in blood flow [6]. Scalar transport in particulate suspensions is a complex process that depends on the transport properties of the constituent solid and fluid phases, as well as operating conditions determined by the applied shear and bounding geometry. Although such particle-laden suspensions are intrinsically two-phase systems, it is often useful to consider them as single media characterized by effective properties. A canonical situation often studied is a particle-fluid system that is confined between two rigid boundaries (see Fig. 1) and exposed to a mean strain rate $\dot{\gamma}$, with particles of diameter d_p occupying fraction ϕ of the total system volume. The particles are assumed non-Brownian and

*Contact author: vinods@umn.edu

 ©2026 American Physical Society

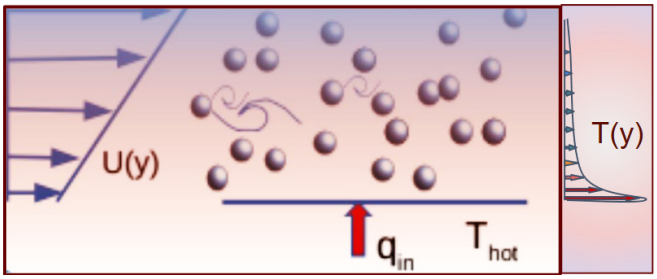

FIG. 1. Sketch of an idealized plane Couette flow of a suspension with heat transfer.

neutrally buoyant in a viscous liquid of kinematic viscosity ν_f and thermal diffusivity α_f. The question of interest is how the effective thermal diffusivity α depends on the above variables.

The augmentation of effective thermal diffusivity due to the combined effects of particle loading and applied shear has been previously surveyed [7]. Much of the understanding of the physical processes responsible for this augmentation has come from the long history of rheological studies [8,9]. The finite size of nondeforming inertialess particles in a shear flow leads to particle rotation, altering fluid stresses and thereby affecting other particles. When a shear field is applied, particles may come close to each other and experience hydrodynamic forces, or collide, leading to displacements that depend on the specific configuration. The random nature of these multiple individual interactions leads to a net diffusive motion referred to a shear-induced diffusion [10,11]. Further, dense suspensions exhibit normal stress differences, unlike simple fluids. These normal stress differences in suspensions under nonuniform flows can cause particles to migrate from regions of high shear to low shear, a phenomenon known as shear-induced migration [11–14]. Recently, Souzy *et al*. [15] have experimentally illustrated the various mechanisms that determine scalar transport. They show that, unlike the linear stretching of material lines in a pure fluid, material lines of a scalar are stretched exponentially in the presence of particles, due to localized variations in strain rate established by particle motion. They also visualize the transfer of scalars from one side of a particle to the other through particle rotation, a mechanism that was previously hypothesized and studied by Wang *et al*. [16] and Ahuja [17,18].

The net effect of these mechanisms is to enhance the apparent thermal diffusivity of the medium α, represented as an enhancement over the zero-shear value, $\alpha^* = \alpha/\alpha_0$. We restrict initial discussion here to the case of negligible particle inertia, expressed in terms of a restriction on the particle Reynolds number ($\mathrm{Re} = \frac{\dot{\gamma} d_p^2}{\nu_f} \ll 1$). Based on dimensional arguments, it can be shown that the enhancement in diffusivity for a suspension of fixed ϕ depends solely on the Peclet number, $\mathrm{Pe} = \frac{\dot{\gamma} d_p^2}{\alpha_f}$ in the Stokes regime. Here Pe is the ratio of the thermal diffusion timescale d_p^2/α_f for the suspending liquid to the advective timescale $1/\dot{\gamma}$. Leal [19] considered the limit of very low Peclet number and arrived at a scaling law of $\mathrm{Pe}^{3/2}$, which was later experimentally verified [20] for a suspension in pure shear flow with $\phi < 0.25$ and $\mathrm{Pe} < 10$. Based on a study of available experiments and modeling, Zydney and Colton [7] suggest a linear dependence of α^* on enhancement, though Fig. 2 in their paper strongly suggests an exponent lower than 1, closer to the value of 0.89 determined by Wang and Keller [6] in their measurements with hardened nondeforming erythrocytes.

Measurements by Metzger *et al*. [21] for $\mathrm{Pe} < 100$ indicate that for low volume fractions ($\phi < 0.4$), the enhancement in thermal diffusivity is consistent with linear dependence on both ϕ and Pe. The authors do note that the best fit to their data was achieved with a power-law fit, $\alpha^* \sim \mathrm{Pe}^{0.88}$. For $\phi > 0.4$, there was a decrease in α, which was attributed to steric effects hindering particle diffusion. Their measurements were taken in a Taylor-Couette cell with a large annular gap (12 mm) relative to the radius (50 mm) of the inner rotating cylinder, leading to strong streamline curvature and

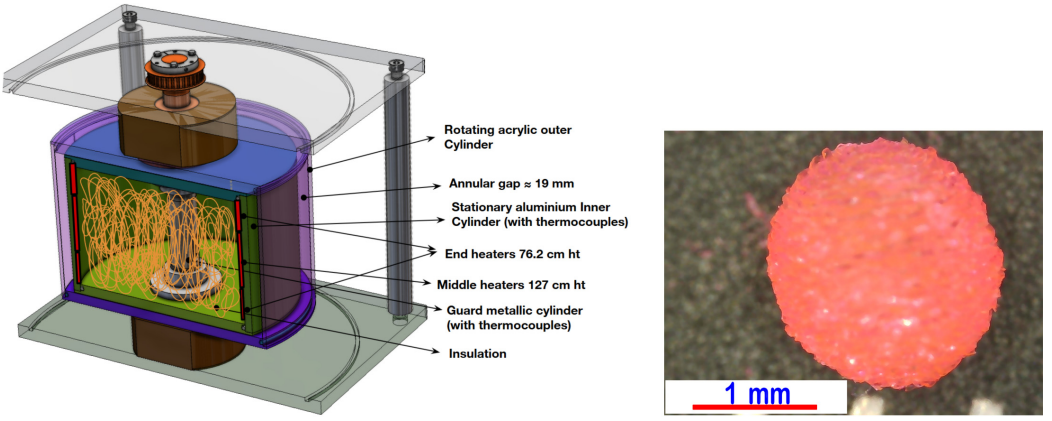

FIG. 2. (a) Schematic diagram of experimental setup: Taylor Couette cell with heater (b) example of a three-dimensional printed particle used.

potential shear-induced migration, possibly enhancing radial transport at low Pe and also leading to their observations of particle layering for higher ϕ.

Existing theory for larger Pe has not been systematically tested. For a dilute suspension with a very high Peclet number, Nir and Acrivos [22] predicted a scaling of $\mathrm{Pe}^{1/11}$ by calculating the sum of flow-induced contributions due to closed isothermal streamlines around each particle. Nadim *et al.* [23] modeled the case where particle interactions are dominant, by considering a two-dimensional array of closely packed cylinders, and arrived at a scaling of $\alpha^* \sim \mathrm{Pe}^{1/2}$ for high Pe. Measurements over a larger range of Pe are available for a limited range of ϕ, mainly for the case of outer cylinder rotation and do not show consistent results. For measurements in a thin-gap Taylor-Couette cell and $\phi = 0.15$ and 0.3, Sohn and Chen [24] observed the scaling $\alpha^* \sim \mathrm{Pe}^{1/2}$ over the range $300 < \mathrm{Pe} < 2000$. Shin and Lee [25] measured steady-state heat transfer in a thin gap Taylor-Couette cell with outer cylinder rotation for low volume fractions ($\phi \leqslant 0.1$) and found an effective thermal conductivity that increased with shear rate and particle size similar to Metzger *et al.* [21]. At higher Pe, they observed a plateauing of thermal conductivity for all volume fractions.

As the shear rate increases at a fixed volume fraction, the particle Reynolds number increases beyond unity. Additional stresses may be introduced in the fluid due to fluctuating inertial transport in the microscale wakes that form behind particles at these values of Re. Experimental data in this regime are relatively scarce, with the majority of our understanding derived from numerical simulations [13,26,27]. Despite differences in the viscosity calculated from these studies due to different modeling assumptions, they agree on the significant effects of inertia on the increase in apparent diffusivity. A theoretical study by Subramaniam and Koch [28] shows that even for weak but nonzero particle inertia, there are contributions to scalar transport arising from the breakdown of fore-aft symmetry and the disappearance of closed streamlines around particles. However, they predict an enhancement over inertia-less theory only at very large RePe, e.g., at $\mathrm{Pe} = 8800$ at $\mathrm{Re} = 0.3$. A preliminary study by the present authors [29] suggested a threefold enhancement in thermal diffusivity as the particle Reynolds number was increased to 40 from near-zero values.

Computer simulations of heat transfer for neutrally buoyant non-Brownian suspensions are scarce in the literature. Wang *et al.* [30] used the lattice Boltzmann technique to simulate particle-laden flow and a Brownian tracer algorithm for mass transfer in a Couette flow and found linear scaling of transport at low Pe and reduced enhancement as Pe was increased. Metzger *et al.* [21] also used a lattice Boltzmann solver with a passive Brownian tracer algorithm and obtained the experimentally observed linear scaling of α^* with Pe. The DNS calculations of Ardekani *et al.* [31]

mainly address the inertial flow of particles in plane Couette flow. For Re = 0, a linear increase in α^* with Pe was obtained for all but the highest volume fractions. For large ϕ, some saturation with Pe was evident and was ascribed to relaminarization of flow in the channel bulk, leading to poor transport.

From the above discussion, it is apparent that there is uncertainty regarding some key issues on scalar transport. The linear behavior of α^* with Pe is not always encountered, with a nonlinear dependence at high Pe observed in experiments as well as simulations. There remain some differences in behavior that appear to depend on the configuration of the Taylor-Couette cell: inner versus outer cylinder rotation. It has been observed that the introduction of particles into a shear flow can drastically alter the critical Reynolds numbers for transition from laminar flow [32]. An inner rotating cylinder that creates the shear is more susceptible to centrifugal instabilities [33], while transition is delayed for outer cylinder rotation [34,35]. The available data also reflect potential effects of gradients in curvature and particle size effects relative to channel dimensions. Further, the mass transfer measurements of Ref. [30] and others do not directly translate into heat transfer, due to the additional available pathway through particles in the case of heat transfer.

We address these issues by performing heat transfer measurements in a thin-gap Taylor-Couette cell with outer cylinder rotation. This configuration is known to extend the laminar regime against centrifugal instabilities [33], allowing a greater range of Pe to be covered, and the thin gap ensures no significant effects of shear-induced migration. We employ a transient temperature measurement technique similar to Ref. [21] to extract the thermal diffusivity by monitoring the temperature response at the inner heated cylinder after a thermal pulse is applied. These measurements are complemented by limited particle velocity measurements using an optically clear outer cylinder.

This article is organized as follows: Section II provides details of the Taylor-Couette cell used for visualizing particle flow and measurements of heat transfer. Section III documents the heat transfer behavior as a function of volume fraction and Peclet number. Section IV contains a brief discussion and summarizes the results.

II. EXPERIMENTS

A. Test facility

The experimental investigation was conducted using a Taylor-Couette cell consisting of a transparent acrylic outer cylinder and a stationary inner cylinder made of galvanized aluminum for fluid heating. The gap between these cylinders is filled with the fluid or test suspension. The outer cylinder has a radius $R_o = 222$ mm, while the inner cylinder has a radius of $R_i = 203$ mm, creating a 19-mm annular gap and yielding a radius ratio $R_i/R_o = 0.914$ that ensures curvature effects are suppressed. The height of the cell is $H = 279.4$ mm, resulting in a height-to-gap ratio greater than 14. For these geometric ratios and outer cylinder rotation, transition to turbulence for pure fluid is expected to occur at a gap Reynolds' number of 4.8×10^3 [36]. For particles of diameter 2 mm (described subsequently), the annular gap is 9.5 times the particle diameter.

The inner cylinder is divided into three heating sections in the longitudinal direction: two end sections of 76.2 mm each at the top and bottom and a central section of height 126.6 mm. The inner curved surfaces of these sections were fitted with flexible silicon heaters for precise temperature control. This configuration enabled independent control of power input to account for potential end effects while maintaining a uniform wall temperature through the height of the inner cylinder. The cylinder is insulated on its inner side with glass wool, directing heat into the fluid. Additionally, a guard metal cylinder at the core of the inner cylinder contains seven thermocouples to monitor potential heat loss.

Twelve calibrated thermocouples, embedded close to the outer surface of the inner cylinder, measure the temperature profile along the cylinder's height and circumference. These thermocouples, calibrated against a standard platinum resistance thermometer to an accuracy of 0.1 K, are distributed spatially to assess the degree of temperature nonhomogeneity across the cylinder surface.

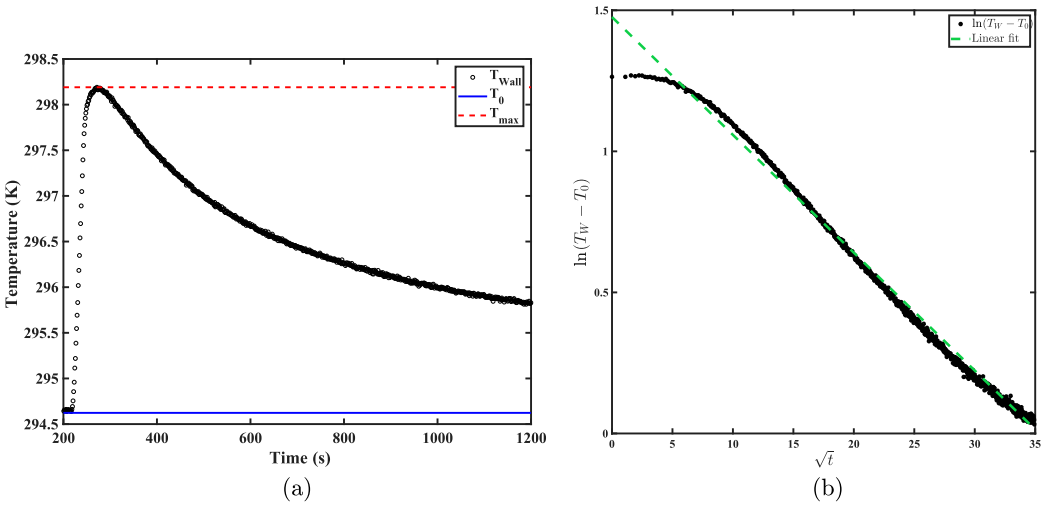

FIG. 3. (a) A typical transient temperature profile of the central section of the inner wall obtained for pure glycerol (b) logarithmic representation of the data to facilitate extraction of the diffusivity using Eq. (3).

Six thermocouples are placed circumferentially in the central section, while three thermocouples monitor temperature in each end section. Temperature data are collected via a Keithley 2701 digital multimeter interfaced with a Python program. In all experiments, the spatial variation of temperature within the test section was found to be below the thermocouple uncertainty of 0.1 K.

The outer cylinder is rotated by a stepper motor, capable of a maximum torque of 21 N m and digitally controlled to provide an angular step resolution of 1.8° and 0.01 rpm speed resolution ($\dot{\gamma} = 1.12 \times 10^{-2}\ \mathrm{s}^{-1}$). An 80-V power supply with a 9-A current is used for the experiments. Some tests also employed a 20:1 gearbox to facilitate smoother operation, with no impact on measurement accuracy.

B. Thermal diffusivity measurement

A transient heat transfer measurement technique is used to determine the thermal diffusivity of the effective medium in the gap. Prior to establishing the desired shear rate required for the heat transfer measurement, the outer cylinder is rotated at the highest speed possible for at least 2 h before the experiment to ensure all particles are suspended uniformly in the media. The experiment begins with setting a predetermined rotational speed of the motor system. The cell runs for 45 min for a desired shear rates below 5 rpm and around 20 min for 5 rpm and above. This is to ensure steady-state flow behavior of the suspension before thermal measurements. All three heaters are turned on simultaneously for 18 s, during which a 3 K temperature rise is observed. Simultaneously, temperatures from the top, middle, and bottom sections are recorded at 9 Hz. Following a procedure similar to that of Metzger *et al.* [21], the decay in temperature at the inner cylinder wall is used to obtain the thermal diffusivity of the medium. A one-dimensional (1D) transient heat-conduction model for the inner wall with a semi-infinite medium was employed. For a constant wall temperature, the exact temperature profile is given by

$$\frac{T_w - T_0}{T_{\max} - T_0} = \mathrm{erf}(x/\sqrt{\alpha t}). \tag{1}$$

Here T_w is the wall temperature, T_0 is the temperature of the suspension medium far from the wall, and $T_{\max}$ is the maximum temperature attained by the wall at the end of the thermal pulse [see Fig. 3(a)]. The inner cylinder temperature measurement after the pulse of heat follows an

exponential decay as previously approximated [21],

$$\frac{T_w - T_0}{T_{\max} - T_0} = e^{-A\sqrt{t}}. \tag{2}$$

The slope of the logarithmic graph in Fig. 3 [$-A$ in Eq. (2)] can be used to derive the thermal diffusivity of the fluid medium if wall density ρ_w, thickness b_w, specific heat C_w, suspension density ρ, and specific heat C_s are known. Here c is a constant, equal to $\sqrt{\pi}$ in the analytical solution,

$$\alpha = \left[\frac{Ac\rho_w b_w C_w}{2\rho C_s}\right]^2. \tag{3}$$

Care was taken to establish repeatable experimental conditions, such as neutral buoyancy and steady-state flow. The overall uncertainty in the measurement of thermal diffusivity was calculated by propagating the raw measurement uncertainty as well as assigned uncertainties in material properties and dimensions through the equations above. The independent effects of these uncertainties were calculated by taking the partial derivatives of derived quantities, calculating the individual uncertainty due to each quantity and then taking the root-mean-square of all uncertainties to arrive at a total uncertainty for the derived quantity, the thermal diffusivity. Uncertainty in the inferred values of thermal diffusivity arises from the following sources: (i) uncertainty in temperature measurement, (ii) uncertainty in the determination of the slope from the logarithmic fit to temperature decay, and (iii) uncertainty due to scatter from repeat trials. The third factor was the most significant, accounting for nearly all of the observed average uncertainty of 11%.

The experimental procedure and data analysis were first validated using a standard Newtonian fluid—reagent-grade glycerol with a thermal diffusivity of 9.22×10^{-8} m^2/s at 25 °C [37]. Using the known thickness of the inner cylinder wall as well as the thermal transport properties of the wall and glycerol [38], we obtain the constant c in the expression for thermal diffusivity [Eq. (3)] as $c = 1.70$, which is approximately 4% less than the expected value, $\sqrt{\pi} = 1.77$. The thermal diffusivity extracted from measurements on the top and bottom heaters differed by less than 10% from that determined from the central section. Buoyancy-driven convection effects along the vertical cylinder wall were considered by calculating a Rayleigh number based on fluid properties and the cylinder height, yielding a value of 1.10×10^7, corresponding to the early laminar stages of free convection. The Richardson number $\frac{g\Delta\rho H}{\rho U^2}$, where U is the outer cylinder rotational velocity, is used to assess the relative strength of buoyancy to imposed inertia and has values spanning the range from 11 at Pe = 10 to 0.008 at Pe = 1500.

C. Suspension medium

In order to ensure a monodisperse particle size distribution, the particles for the suspension were 3D printed with a commercial 3D printer. From measurements of the particle size distribution, the acrylic particles were found to have a mean diameter of 1.93 mm and a standard deviation of 0.1 mm. The particles had a nominal density of 1180 kg/m^3. The surface roughness of the particle closely matched the resolution of the 3D printer, of about 25 μm, yielding a roughness-to-diameter ratio of 0.0125. The base fluid was a 57/43 v/v mixture of glycerol and propylene glycol. This ratio was arrived at by preparing small batches of suspension and checking for neutral buoyancy over long times, typically of the order of several hours. Some particles exhibited buoyancy, presumably due to void formation during the printing process, and were removed. The dynamic viscosity of the base fluid was measured and found to be 266 mPa s. A differential scanning calorimeter was used to measure the specific heat capacity of the base fluid, which was found to be 2.665 kJ/kg K.

D. Flow visualization

Flow visualization was performed in the circumferential θ-z plane of the outer cylinder using particle tracking velocimetry with high-speed imaging. The base fluid was dyed with

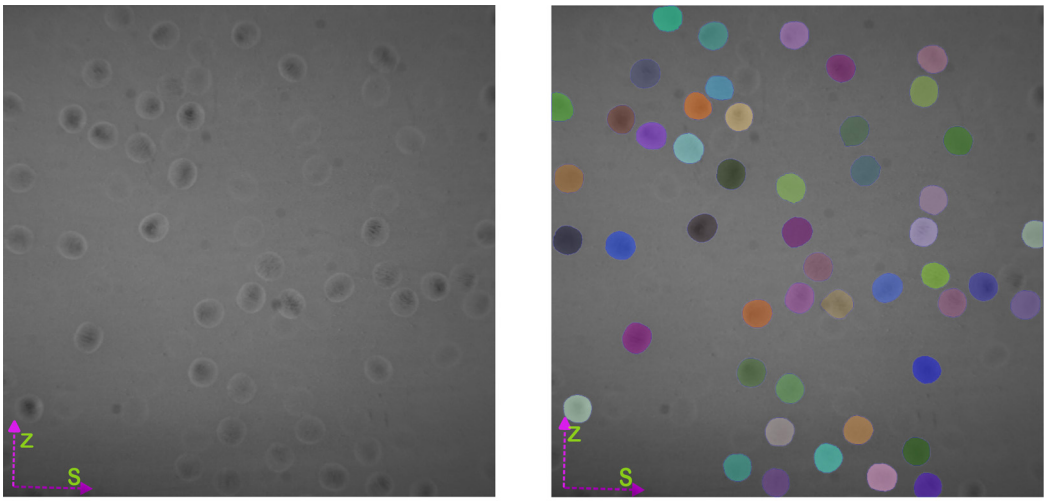

(a) (b)

FIG. 4. Visualization steps: (a) Raw image for $\phi = 14\%$ at 20 rpm and (b) segmented image showing labeled particles. Both images show an area of 30 cm $\times$ 30 cm.

rhodamine-6G to make the particles appear as black circles against a bright fluid background. The middle section of a 30 cm $\times$ 30 cm cross section of the Taylor-Couette (TC) cell was illuminated by a light sheet generated using a 6.5-W LED light source operating at 532 nm, and video recordings were made with a Photron mini AX100 camera equipped with an orange filter. The images of dimension 1024 $\times$ 1024 px yielded a resolution of 0.29 mm/px and were processed to yield particle positions, displacements, and velocities.

The Segment Anything Model 2 (SAM 2) code [39] was used to segment images and to estimate the centroids of particles from a nonuniformly lit image stack. The nonuniformity in the illumination is due to the dispersion of light through the rough particle media. For each image stack of approximately 900 images, centroid-based segmentation was applied to the first image, and particles were manually labeled with a unique identifier (see Fig. 4). The segmented area was filtered with size expectation-based filtering, using segments of size equal to at least half a particle diameter and no more than a quarter of the image area. The SAM 2 video segmentation expects to see all objects to be tracked in the first image of a stack. Therefore, segmentation is performed on the first image of the stack to identify centroids. Image processing was performed in stacks of 20 images (chosen so as to have the first particle tracked until it leaves the frame). SAM 2 gives the centroid location of the particle in the next 20 images by using its machine learning algorithm. The procedure is repeated for the next image stack derived by dropping the first image and adding an image at the end. Thus, any new particles entering the field of view are automatically labeled. Centroid locations repeated in any frames are considered as particles identified previously and the same object identifier number is used. Particle velocities are calculated using centroid locations obtained between image pairs. Filtering functions are applied to the velocities to further eliminate outliers. A standard deviation-based filter defined using upper and lower bounds on the particle velocity is used in conjunction with a median absolute deviation filter.

III. RESULTS

Prior to experiments with sheared suspensions, the zero-shear diffusivity of each suspension was measured in the TC cell for $\phi = 0.14$, 0.22, 0.30, and 0.35. Figure 5 shows the variation of this value with volume fraction. The specific heat of PMMA is 55% of the base fluid, with the result that

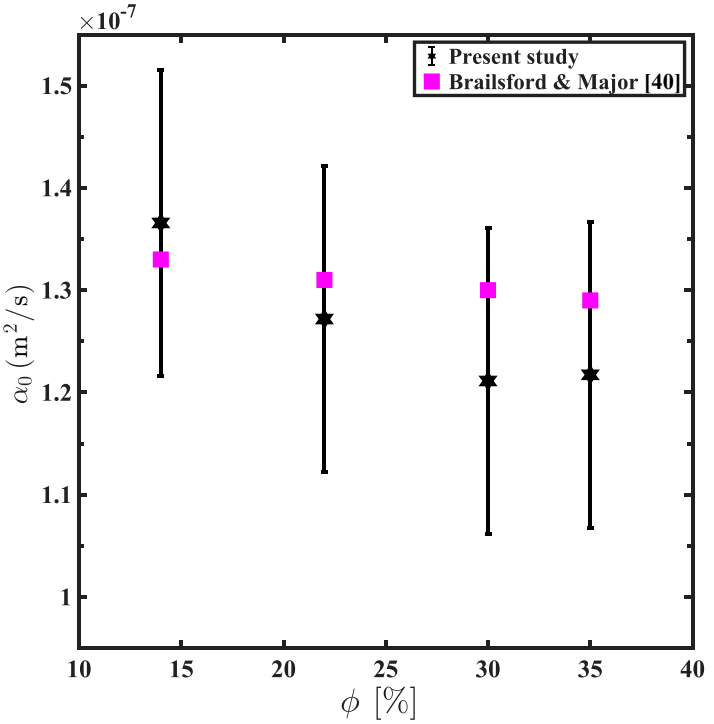

FIG. 5. Zero shear experimental thermal diffusivity (α_0) compared to expected Brialsford Major's Model values [40].

particle loading does not substantially depress the zero-shear diffusivity from that of the base fluid for any volume fraction studied. Also plotted are estimates of the suspension thermal diffusivity, calculated from the model of Brailsford and Major [40], which assumes a uniform distribution of particles of volume fraction ϕ in a fluid medium. The measured data and predicted values are in good agreement when their respective uncertainties are taken into account.

A total of 103 test cases (specified by combinations of Pe and ϕ) were performed, with 34 done at the lowest volume fraction $\phi = 14\%$, 26 cases at $\phi = 22\%$, 18 cases at $\phi = 30\%$, and 25 cases at $\phi = 35\%$. Figure 6 shows the entire dataset in the form of thermal diffusivity α normalized by the corresponding zero-shear diffusivity α_0 for the entire range of Pe studied. Three distinct regimes of behavior are evident: (i) a roughly linearly increasing behavior for low Pe < 100, (ii) a region of reduced enhancement for $100 <$ Pe < 1000, and (iii) a regime where the enhancement appears to be a very weak function of Pe at the highest Pe studied. The trend appears similar for all values of ϕ, though the enhancement is substantial for the highest value of $\phi = 0.35$. We now examine each of these Pe ranges in greater detail.

Figure 7 shows the enhancement in effective thermal diffusivity over the zero-shear value for various volume fractions $\phi = 0.14$, 0.22, 0.3, and 0.35 for Pe < 100 (Re < 0.06). Each data point shown is obtained by averaging out typically three runs with data acquired from four thermocouples in the midsection. There is a broadly linear trend apparent with Pe, and fitting linear behavior to the data results in the correlation $\alpha^* - 1 = 0.0039\text{Pe}$, where the constant prefactor indicates the low variation in enhancement with volume fraction. However, the best fit to the data is a power law with an exponent of 0.91 ($\alpha^* - 1 = 0.0054\text{Pe}^{0.91}$), though the difference in root-mean-square deviation of the points from the data differs by less than 1% for the two relations. We note that Metzger *et al.* also find a power-law exponent of 0.88 to be the best fit. The dependence on volume fraction is less distinct due to the low level of enhancement of α^* at any value of Pe < 100, which is a result

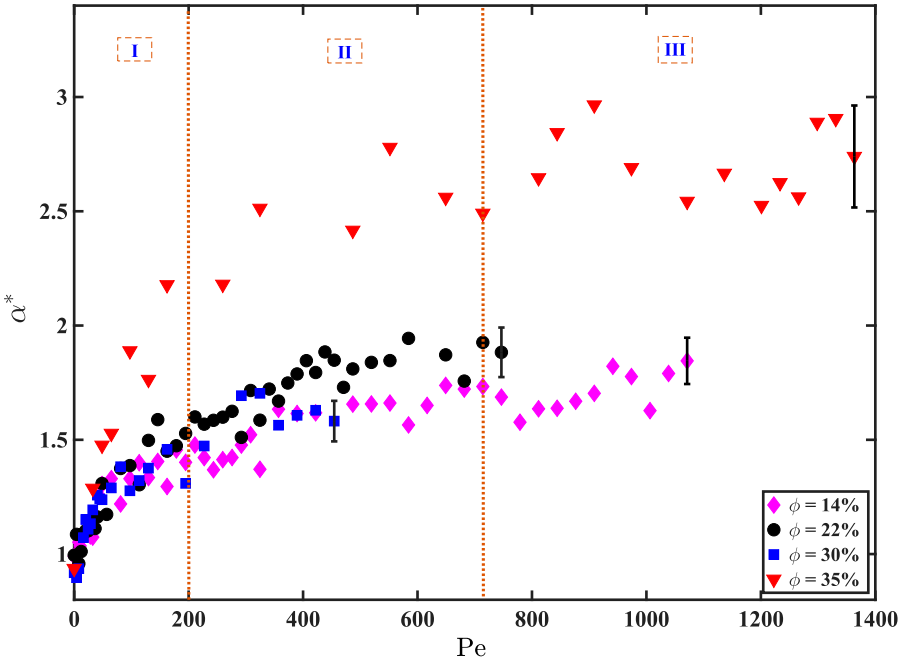

FIG. 6. The entire dataset of measurements showing variation of α/α_f for Pe $<$ 1400. The error bars shown at the highest Pe value are representative of each dataset.

at variance with that of Metzger *et al*. [21], who observe a linear increase in α with ϕ for volume fractions less than 0.4. Figure 7(a) shows individual fits for the different volume fractions, with only the highest volume fraction attaining a significant enhancement relative to the lower volume fractions.

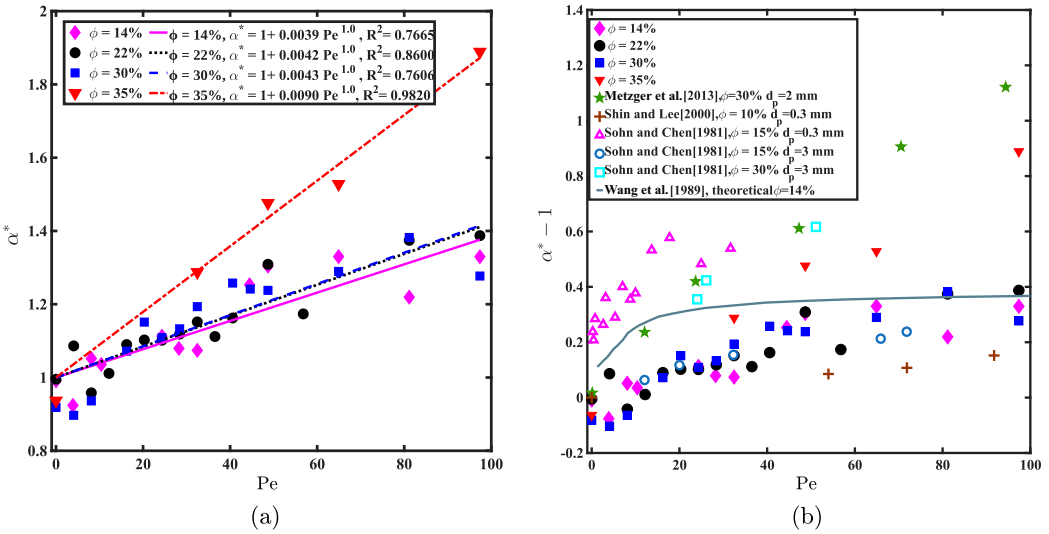

FIG. 7. (a) Linear fits to the data for each volume fraction for Pe $<$ 100. (b) Comparison of the data for Pe $<$ 100 with the data of Shin and Lee [25], Sohn and Chen [24], and Metzger *et al*. [21].

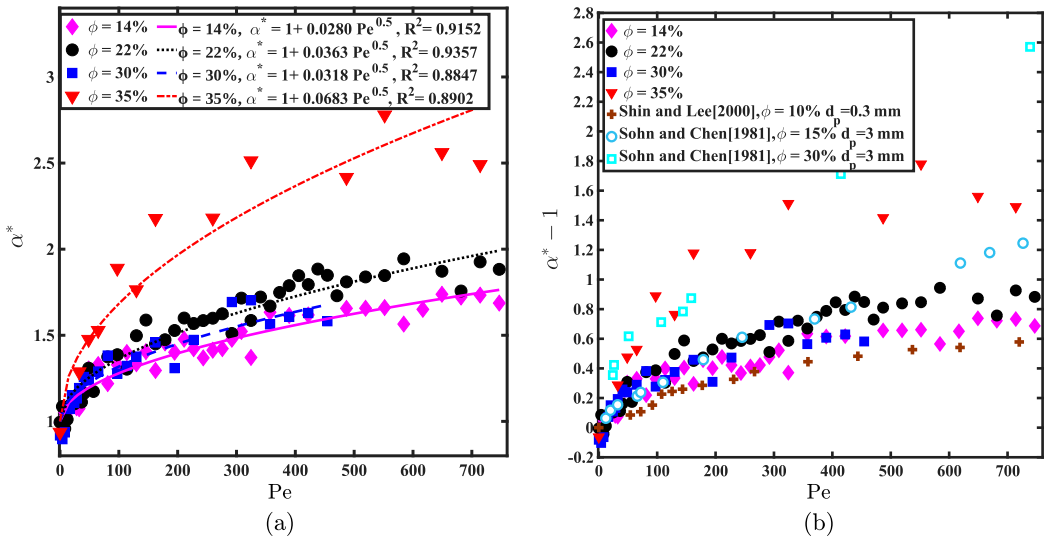

FIG. 8. (a) Variation of effective thermal diffusivity for multiple volume fractions as a function of Peclet number Pe (b) comparison of the data for Pe < 800 with the data of Shin and Lee [25], and Sohn and Chen [24].

Figure 7(b) compares the data for Pe < 100 with data available in the literature. The data from Shin and Lee [25] that are most appropriate for comparison correspond to their largest diameter studied (300 μm) and the highest ϕ of 0.1. The data of Metzger *et al.* [21] and Sohn and Chen [24] are, in general, higher than the data from the present study and those of Shin and Lee. Notably, the ratio of the mean radius of the annular gap to the gap width for these two studies was approximately 4 and 4.8, respectively, while those of Shin and Lee and the present study are approximately 10, potentially hinting that strong curvature effects may be present in the data of Sohn and Chen and Metzger *et al.* [21]. The data of Sohn and Chen also show a strong dependence on particle size, suggesting confinement effects. For the lowest volume fraction of 14%, the theoretical predictions of Wang *et al.* [16] for dilute suspensions are in surprisingly good agreement with the present measurements.

A. Intermediate regime of Peclet number

As the value of Pe is increased substantially beyond 100, the nonlinear variation of the diffusivity enhancement becomes strongly apparent. Figure 8 shows that the enhancement in α^* starts increasing at a slower rate in the range $100 < \mathrm{Pe} < 700$, with the particle Reynolds number varying in the range $0.06 < \mathrm{Re}_p < 0.42$. While there is a roughly 40% enhancement as Pe increases from 0 to 200, an additional enhancement of 40% over the zero-shear value is achieved only when Pe is quadrupled to 800. The variation for the three lower volume fractions is well captured by a power law with a best-fit exponent of 0.50. For the highest volume fraction of $\phi = 0.35$, the enhancement is higher, though the variation at high Pe is still well captured by a 1/2 power law. Figure 8(b) shows a subset of the present data ($\phi = 0.14, 0.30$) for comparison with the literature. The data of Sohn and Chen [24] for $\phi = 0.15$ and 0.30 also follow a 1/2 power law for large Pe, while the data of Shin and Lee for $\phi = 0.1$ exhibit a saturation in enhancement as Pe is increased.

While theories exist that predict an effective 1/2 power scaling with the Peclet number [23], these involve the assumption that the entire system can be modeled as being filled with large bodies of revolution that are closely packed, with the resulting flow-field being dominated by lubrication interactions. In the present case, the 1/2 power-law behavior is observed even for the lowest volume

fraction of 0.14, and therefore, we need to look for a different explanation. One mechanism that has been proposed to explain this nonlinear behavior is the formation of a particle-free layer near the inner wall. The presence of such a particle-free layer near the inner wall has long been inferred [41] and recent measurements in TC cells with inner cylinder rotation have documented particle migration away from the inner wall [42–44]. In principle, for spherical particles that have point contact with the wall, the volume fraction goes down to zero at the wall, and any loss of point contact due to radial migration of particles increases the effective thickness of this fluid layer. Wang *et al*. [30] have observed this 1/2 power-law scaling in their steady-state measurements of solute diffusion in an electrochemical cell. Their lattice Boltzmann simulation of point tracers predicted results consistent with the formation of two fluid layers on the inner and outer cylinders. In the present study involving a transient temperature measurement, it is likely that the temperature at the inner wall does not respond to the formation of a fluid layer on the outer cylinder, and therefore we consider the situation of a layer of a suspension medium bounded by a particle-free fluid layer of thickness δ, where the thickness may in principle be a function of the Peclet number Pe, possibly as a power law of the form $\delta = A\mathrm{Pe}^n$.

The thermal resistance of this fluid layer is given by δ/k_f. From the measured diffusivity, one can extract the thermal penetration length L_{pen} during the measurement and consider its average value. Modeling the observed effective thermal diffusivity (or, equivalently, conductivity) to be the result of two thermal resistances in series, corresponding to this fluid layer and the particle medium, gives us the expression

$$\alpha^* = L_{\mathrm{pen}}[(A\mathrm{Pe}^{0.06}) + \frac{(C_f/C_sB)}{(1 + (0.0032)\mathrm{Pe})}]^{-1}; \tag{4}$$

The inferred value of the penetration length from experiments varies very weakly over the data range, with an average value of $L_{\mathrm{pen}} = 12$ mm. Then the fitting parameters obtained are $A = 2.59$ mm and $B = 5.76$ mm. Here the resistance of the suspension medium alone at high Pe is conjectured to follow the results at low Pe where particle slip effects are likely less significant. It can be observed from Fig. 9(b) that the linear behavior of α^*, when combined with a fluid layer of thickness δ, matches the measured data quite well when the thickness of the particle-free layer of fluid on the inner wall scales weakly with Pe as $\delta = A\mathrm{Pe}^{0.06}$. Despite the reasonable agreement between the model and the data, we emphasize that the model is constructed on several strong assumptions, including the presence of the particle-free fluid layer, the extension of the low-Pe behavior to high-Pe values, as well as quasistatic diffusion. Further experiments are needed to verify the existence and extent of such a particle-free fluid layer.

Next, the data at high Pe are considered. Nir and Acrivos [22] have arrived at the result $\alpha \sim \mathrm{Pe}^{1/11}$ for large Pe by considering transport solely through particle rotation and considering the existence of closed streamlines around each particle, which act as regions of infinite thermal conductivity in the steady state. Pending the direct observation of a liquid layer near the inner cylinder, we set aside the linear behavior used to derive Eq. (4) and in Fig. 10 we examine the data considering α^* in the range 500–800 for the near-dilute case of $\phi = 0.14$ where the theory applies, as well as for $\phi =$ 0.22. The data have best fit exponents that are not far from 0.09; however, the scatter in the data, especially for $\phi = 0.14$ makes it hard to draw definite conclusions.

We also note that the theory does not consider the diffusive nature of particle motion, which has been well established since the study of Ref. [22] and is likely to enhance transport beyond the 1/11 exponent. Further, at these Pe, the particle Reynolds number Re starts to assume non-negligible values, ranging from 0.42 at $\mathrm{Pe} = 700$ to a value of 0.82 at the highest values studied.

At still higher Pe up to 1000, the 1/2 power-law scaling observed in the range 400–700 continues to hold for the lower volume fractions 0.14, 0.22, and 0.30 (not shown). However, the quality of the fit for $\phi = 0.35$ was found to be significantly reduced over this extended range, with the power-law exponent continuously decreasing from 0.5 to smaller values, as low as 0.3 with increasing range of Pe. When the data in the range $700 < \mathrm{Pe} < 1400$ are normalized by a power-law obtained for $\mathrm{Pe} < 700$ with an exponent of 0.5, it is apparent [see Fig. 11(a)] that the fit does not capture the

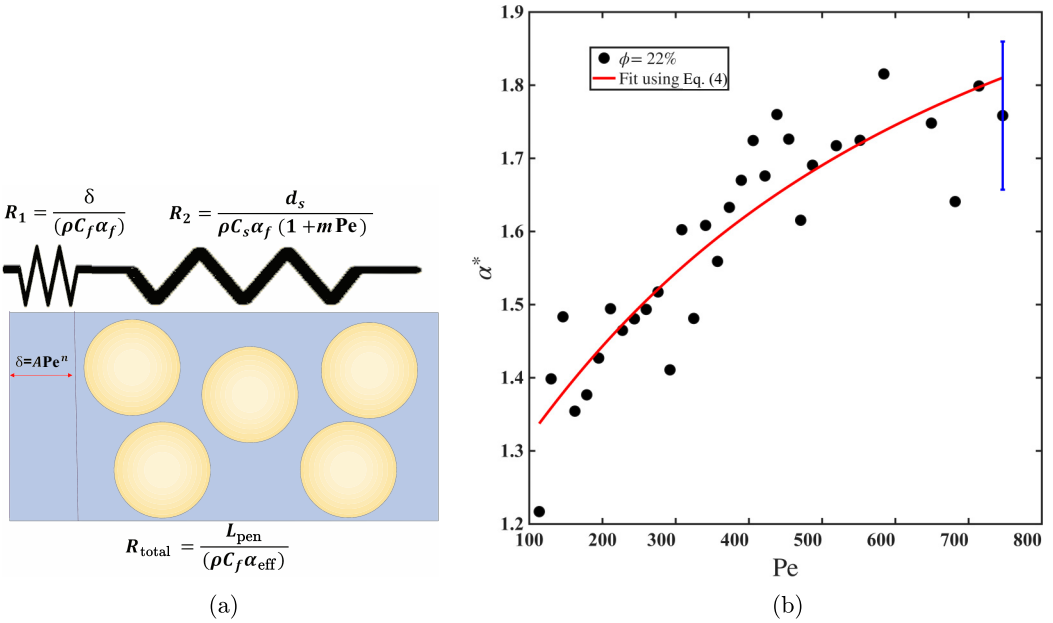

FIG. 9. (a) Sketch of the resistance model from Ref. [30] adapted for a particle-free fluid layer at one wall. (b) Comparison of measured thermal diffusivity over an extended range of Pe with a thermal resistance model. Error bar shown at the highest Pe value is representative of the entire data range.

behavior of the normalized diffusivity. The behavior in this high Pe range shows a weak dependence on Pe is plotted in Fig. 11(b) and shows a power-law exponent close to 0.06. Such near-saturation in α^* was observed by Shin and Lee [25] even for dilute suspensions, though it is not observed in the present dataset. The value of 0.06 is close to that of 1/11 predicted by Nir and Acrivos for the high Pe limit, though it should be noted that the theory holds for dilute suspensions and therefore no inferences can be drawn on the responsible mechanisms from this coincidence.

We note that inertial effects are unlikely to be the cause of this saturation—over this extended range of Pe, the particle Reynolds number Re is significant, ranging from 0.42 to 0.82, and would be expected to cause increased enhancement, not the observed saturation.

B. Measurements of particle motion

Attention is now given to the particle motion that is presumably responsible for the observed enhancement in diffusivity. A question that arises is whether the particles themselves transport the passive scalar through their diffusive motion as well as rotation or whether the enhancement is mainly accomplished through the mixing motion and variable strain fields established in the interparticle regions. To do this, a measure of the particle diffusion characteristics is first sought.

Figures 12(a) and 12(b) show examples of the motion of particles in the circumferential and longitudinal directions, respectively. For the circumferential direction, the diffusive motion is obtained by subtracting the mean circumferential velocity obtained by ensemble averaging the circumferential displacement over 840 image frames. Data shown in Fig. 12 correspond to a shear rate of 3.67 1/s and a Peclet number of 98.

The random nature of the displacements is assessed by calculating the distribution of velocity fluctuations corresponding to these displacements. Figure 13 shows the probability density function (PDF) corresponding to motion in both directions for one value of Pe in the linear regime (Pe = 65.5) and for another where the saturation in diffusivity is evident (Pe = 490.7) for $\phi = 22$. These datasets were obtained by tracking particles over 840 frames in consecutive loops of 50

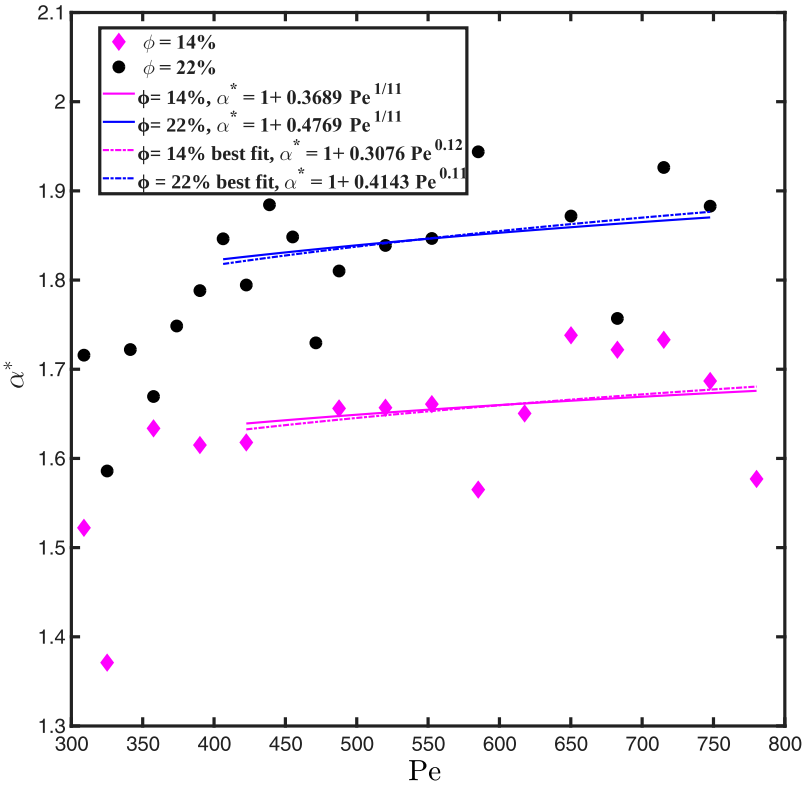

FIG. 10. Comparison of the data at high Pe in the range 500–800 with the 1/11 scaling proposed by Nir and Acrivos [22].

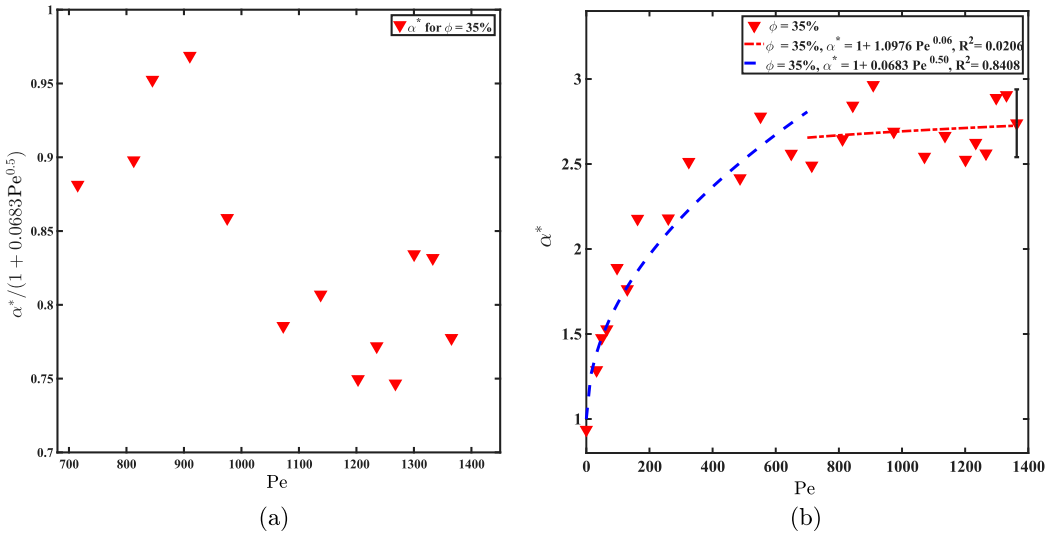

FIG. 11. (a) Enhancement in diffusivity for $\phi = 0.35$ in the high Pe range 700–1400, normalized by the best fit in the range 0–700. (b) Best fit for α^* in the range 700–1400. Error bar shown at the highest Pe value is representative of the entire data range.

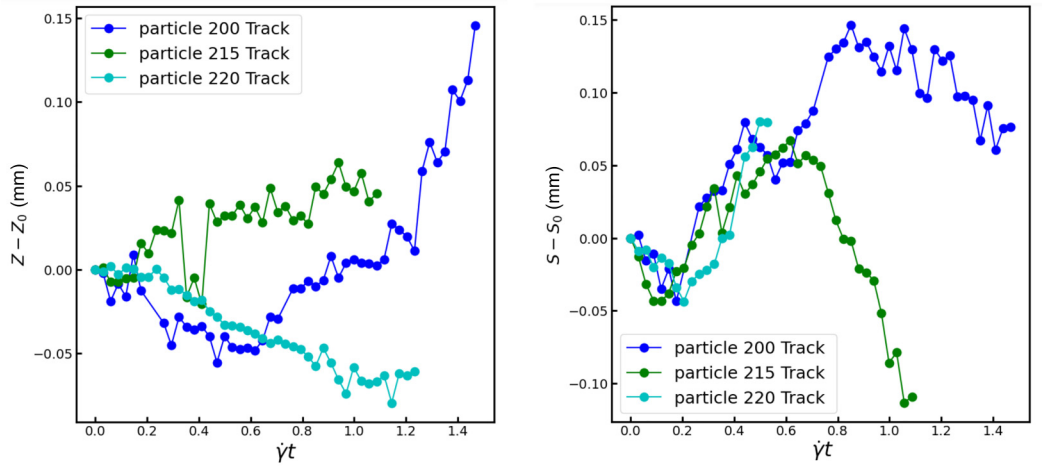

FIG. 12. Particle motion in the (a) axial direction and (b) in the circumferential direction with time-averaged velocities removed to capture diffusive displacements.

and 30, respectively. For both values of Pe, the fluctuations in the axial direction are symmetric [Figs. 13(b) and 13(d)]. However, the circumferential velocities [Figs. 13(a) and 13(c)] show a slight skewness towards lower velocities. A Kolmogorov-Smirnov test was performed to determine if these distributions allowed the possibility of having been sampled from an underlying Gaussian population, and the results were not consistent with that hypothesis. It is not clear if this result reflects possible uncertainties in measurement or whether there are underlying physics that are responsible for the deviation from a Gaussian distribution. It should be noted that in extracting the displacements, the particles are assumed to be one diameter away from the outer cylinder radial location, due to the clear inability of illumination to penetrate further into the medium as a result of light scattering. However, the quantification of the uncertainty inherent in this assumption is difficult, and coupled with the weak but finite nonlinearity in the radial velocity profile, the results must be interpreted with caution.

To address this in a different way, an integral quantity arising from fluctuations is sought, rather than examining the PDF. The irregular motion of the particles is used to evaluate the particle self-diffusivity and compare it to the observed enhancement in thermal diffusivity. We construct the variance of the displacement $\langle(\Delta s)(\Delta s)\rangle$ and $\langle(\Delta z)(\Delta z)\rangle$ for motion in the circumferential and axial directions, respectively, which, for a diffusive process, would be expected to be linearly proportional to the time duration of the random walk process. Expressing this in nondimensional terms by normalizing the variance with the particle diameter d^2 and time by the applied strain rate $\dot{\gamma}$, and plotting the resulting variance quantities yields Fig. 14. The variance is linear with time at long times and is suggestive of particle self-diffusion. After some rearrangement, one may write the particle diffusivities $D_{ss} = \langle(\Delta s)(\Delta s)\rangle/2t$ and $D_{zz} = \langle(\Delta z)(\Delta z)\rangle/2t$ as $D_{zz}/\alpha_f \sim C_z\mathrm{Pe}$ and $D_{ss}/\alpha_f \sim C_s\mathrm{Pe}$. Extraction of the slope from Figs. 14(a) and 14(b) for $\mathrm{Pe} = 65.5$ yields values of $C_S = 2.12 \times 10^{-2}$ and $C_z = 1.33 \times 10^{-3}$, respectively. Noting that α_f differs from α_0 by only a few percentages, one can compare these prefactor values against those from the thermal measurements in the linear regime [0.0028 from Fig. 7(a)]. The particle self-diffusivity D_{ss} appears to be of the same order of magnitude as the thermal diffusivity, suggesting that particle motion may be responsible for some degree of thermal transport, in line with the calculations of Ardekani *et al.* [31] for low Pe. However, the same calculation for a higher value of $\mathrm{Pe} = 491$ [Figs. 14(c) and 14(d)] yields slopes that are one order of magnitude higher than at low Pe, implying a substantial increase in particle diffusion that is not matched by the observed thermal transport. Steric interactions and particle layering have been

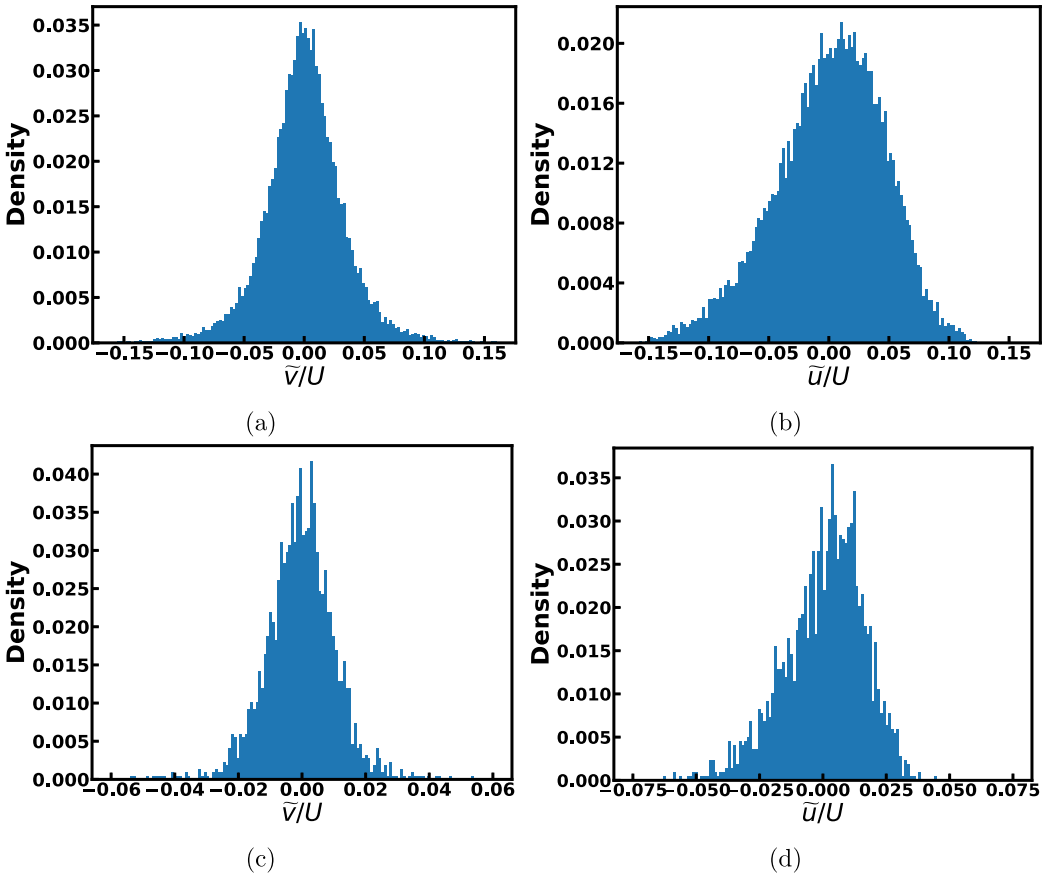

FIG. 13. Probability density of velocity fluctuations normalized by streamwise velocity in the (a) axial and (b) circumferential direction for 2 rpm (Pe = 65.5) (c) axial and (d) circumferential direction for 15 rpm (Pe = 490.7).

proposed as a possible mechanism [21] at higher values of ϕ, though the reduction in enhancement at high Pe is observed for all values of volume fraction. Nevertheless, for each volume fraction, we checked for possible particle layering near the outer cylinder by assessing the average number of particles present in each image as the Peclet number was increased. No significant changes were found, suggesting no significant particle accumulation or migration towards the outer cylinder as the Peclet number is increased.

IV. SUMMARY AND CONCLUSIONS

Thermal diffusivity measurements were performed in a particle-fluid suspension with particle volume fractions of 0.14, 0.22, 0.30, and 0.35. A uniform shear field was imposed in a thin-gap Taylor-Couette cell using outer cylinder rotation, thereby minimizing centrifugal instabilities. Measurements were taken in the Stokes regime as well as the early stages of the inertial regime where the particle Reynolds number is of the order of unity.

The results were compared at low and high Peclet numbers with available theories that predict the limiting behavior as a function of Pe. Linear behavior is found at low Pe, while a 1/2 power law is observed at moderate to high Pe for the lower volume fractions. While some theories predict a 1/2 power-law behavior for high volume fractions and a 1/11 power-law behavior for dilute fractions.

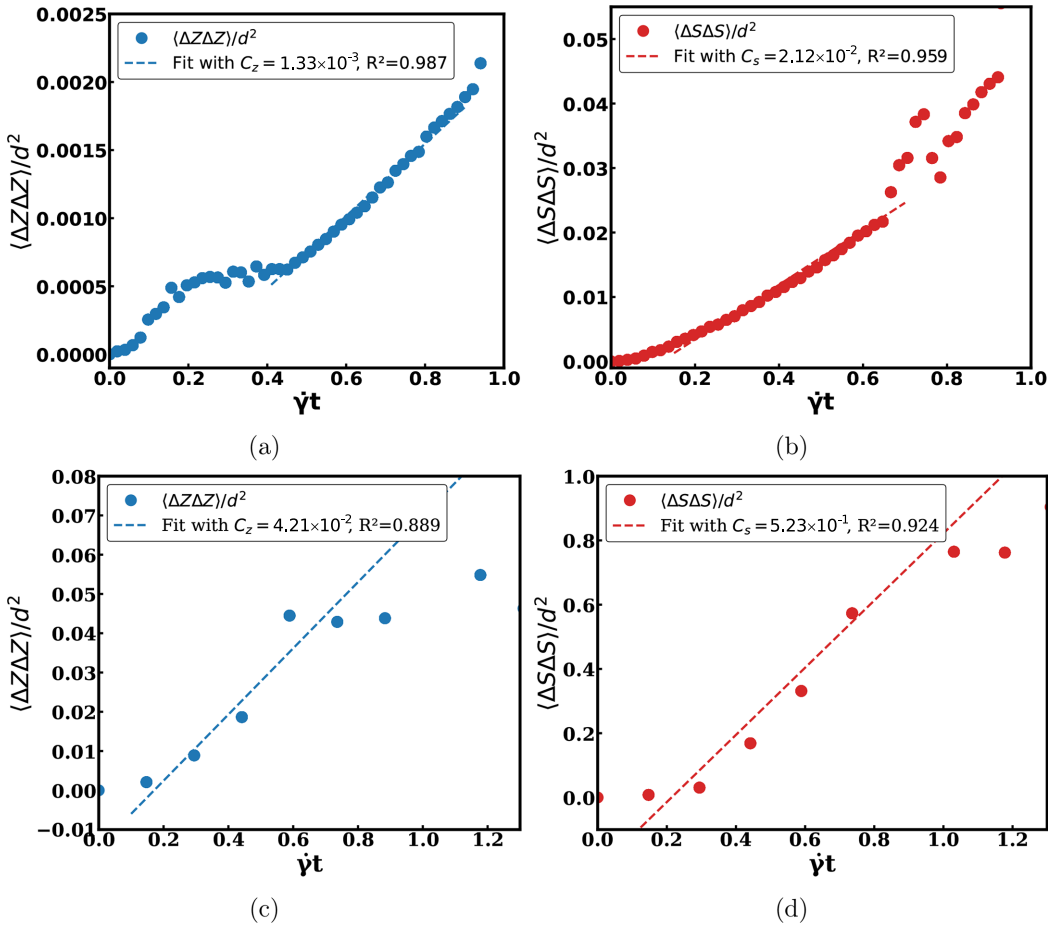

FIG. 14. Nondimensional variance in particle position (displacement squared) as a function of total strain for diffusive motion in the (a) axial and (b) circumferential direction for 2 rpm (Pe = 65.5) and (c) axial and (d) circumferential direction for 15 rpm (Pe = 490.7).

Neither of these behaviors was observed. At the highest volume fraction of 0.35, a 1/2 power law is observed at low to moderate Pe before the enhancement nearly saturates. The data indicating a 1/2 power law were also consistent with the proposed formation of a thin particle-free liquid layer on the inner cylinder wall.

Particle motion was tracked by high-speed imaging and the diffusive motion of particles in the axial and circumferential directions was inferred from the images. Extraction of the particle diffusivity and comparison with the measured thermal diffusivity suggest that the overall transport may have some contribution due to particle diffusion and resulting mixing at low Pe; however, this fails to account for reduced enhancement at high Pe.

We explore whether inertial effects can partially explain this behavior. A Reynolds number based on the annular gap width, the rotational velocity of the outer cylinder and the effective viscosity of the suspension estimated from a standard relation such as the Eilers equation is constructed. This gap Reynolds number attains values up to 45 in the present study and motivates consideration of fluid and particle inertia. While Subramaniam and Koch [28] predict an enhancement in heat transfer even at low particle inertia, provided Pe is sufficiently high, their predicted enhancement scaling [$\alpha^* \sim (\mathrm{RePe})^{1/3}$ plus higher-order corrections] does not match the observed scaling. Their scaling

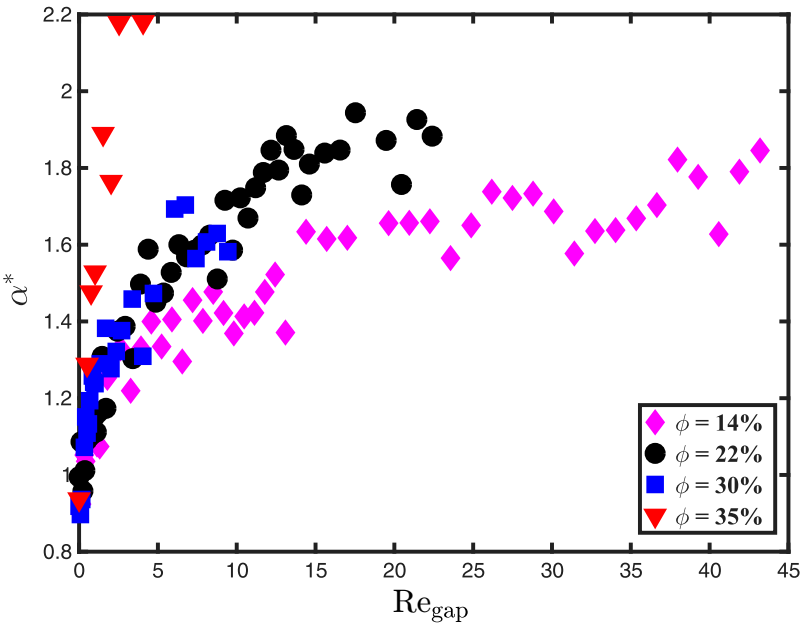

FIG. 15. Enhancement in thermal diffusivity plotted as a function of the annular gap Reynolds number $\frac{\dot{\gamma}(R_2-R_1)^2}{\nu}$, with the kinematic viscosity of the suspension ν calculated from Eilers equation [9].

predicts a power-law dependence of diffusivity on the imposed shear rate with an exponent of 2/3, which is at variance with the observed exponent of 1/2 for Pe $<$ 1400. We also note that they predict an enhancement over the case of zero inertia at much higher values of PeRe (2450) than attained in this study, around 1120.

Migration of particles in a direction transverse to fluid streamlines under weak inertia and variable strain fields has been previously studied [45–47]. Recent studies in the TC cell geometry by Morris and co-workers [42,43] as well as others [44] have visualized the role of inertial migration of particles in the radial direction. They have shown that the presence of particles in a TC flow and their migration, as well as the particle size and volume fraction, have several important consequences for the Taylor-Couette flow that go beyond affecting the local particle distribution and resultant viscosity profile. In particular, a lower critical gap Reynolds number (relative to pure fluid) marking the transition of flow from circular Couette flow to other flow regimes was observed. At first glance, it is worth questioning the relevance of these results to the present study, which has outer cylinder rotation and, according to the regime map for onset of instabilities for pure fluid [48], should be stable at all shear rates. Recent studies by Alam and co-workers [49,50] for co-rotating and counter-rotating cylinders also suggest the stability of TC flow with only outer cylinder rotation, even with particles. However, as the above studies also show, the presence of particles is inherently destabilizing, and the transition in flow structure was a strong function of the particle size with substantial reduction in the critical Reynolds number even for particle sizes of 230 μm (1/30 of gap width in Ref. [43]). In the present case, the particles are much larger relative to the channel width and the effect of finite disturbances cannot be ruled out. Figure 15 plots the thermal diffusivity values as a function of the annular gap Reynolds number, with the suspension viscosity estimated using the Eilers equation $\mu = \mu_f[(1 + 5\phi/4)/(1 - \phi/\phi_c)]^2$ [9]. While no obvious transitions are seen for the higher volume fractions, a distinct break in the data is seen for $\phi = 0.14$ at Re $\sim$ 31, whose origin is currently presumed to be random noise but warrants further investigation. Given the dearth of studies that examine particle motion with outer cylinder rotation, this is an area ripe for further study.

In summary, the observed thermal diffusivity behavior, including its weak saturation at high Pe and ϕ cannot be explained by existing theory. While shear-induced migration arising from interparticle interactions may enhance particle transport in the radial outward direction, even with outer cylinder rotation, these effects may possibly be counteracted by inertial migration of particles at higher Re. This in turn depends on whether particles lag or lead the local fluid velocity, established with an altered particle distribution due to shear-induced migration. While inertial migration has been documented for planar flows and for TC cells with inner cylinder rotation, little information exists on TC cells with outer cylinder rotation or at high particle concentrations, and therefore their combined effects on an effective diffusivity of particles is an open question.

Souzy *et al*. [15] have shown through detailed visualization that increased shear and accompanying particle rotation does not necessarily stretch material lines everywhere and that locally increased concentrations of scalars can also occur, though overall transport is driven by the complex strain field established between particles. Following Souzy *et al*. [15], it is tempting to consider whether the overall diffusivity of the medium can be modeled to be of the form $\alpha = \phi\alpha_{pm} + (1-\phi)\alpha_f$ where the two terms on the right-hand side refer to transport contributions from particle motion and thermal diffusion in the fluid, respectively. Indeed, the DNS calculations of Ardekani *et al.* [31] suggest that even at particle Reynolds numbers as high as 0.5, the major contribution to thermal transport arises from fluid thermal diffusivity acting on sharp temperature gradients established by particle motion, with particle motion itself contributing a lesser but nonnegligible amount. The present dataset supports this conclusion, with particle motion being a smaller contributor than in the above DNS calculations.

The significant caveat to these inferences is that the appropriate particle diffusivity for comparison with thermal diffusivity should be extracted from diffusive motion in the radial direction. Unfortunately, the metal inner cylinder and rotating outer cylinder make it difficult to use techniques such as refractive index matching to observe particles in the radial plane. One may expect particle diffusivity in the circumferential and axial directions (i.e., not in the radial plane aligned with the direction of shear) to be equal valued in the bulk. However, this assumption too is likely to break down near the outer cylinder, and this is confirmed by the markedly different values of particle diffusivity apparent in the slopes of Figs. 14(a) and 14(b). A future study will address this issue through appropriate modification of the test facility to enable imaging in the radial plane.

ACKNOWLEDGMENT

We gratefully acknowledge partial support for this work from the American Chemical Society-Petroleum Research Fund (Grant No. 66772-ND9).

DATA AVAILABILITY

The data that support the findings of this article are not publicly available. The data are available from the authors upon reasonable request.

[1] C. Qian and G. Gao, Reduction of interior temperature of mass concrete using suspension of phase change materials as cooling fluid, Constr. Build. Mater. **26**, 527 (2012).
[2] A. Kijo–Kleczkowska, Combustion of coal–water suspensions, Fuel **90**, 865 (2011).
[3] R. L. Wu, J. R. Grace, C. J. Lim, and C. M. Brereton, Suspension-to-surface heat transfer in a circulating-fluidized-bed combustor, AIChE J. **35**, 1685 (1989).
[4] B.-S. Kang, S. G. Kim, and J.-S. Kim, Thermal degradation of poly (methyl methacrylate) polymers: Kinetics and recovery of monomers using a fluidized bed reactor, J. Anal. Appl. Pyrolysis **81**, 7 (2008).
[5] J. Dufek, The fluid mechanics of pyroclastic density currents, Annu. Rev. Fluid Mech. **48**, 459 (2016).

[6] N.-H. L. Wang and K. Keller, Augmented transport of extracellular solutes in concentrated erythrocyte suspensions in Couette flow, J. Colloid Interface Sci. **103**, 210 (1985).
[7] A. L. Zydney and C. K. Colton, Augmented solute transport in the shear flow of a concentrated suspension, Physicochem. Hydrodynam. **10**, 77 (1988).
[8] A. Einstein, Effect of suspended rigid spheres on viscosity, Ann. Phys. **324**, 289 (1906).
[9] É. Guazzelli and O. Pouliquen, Rheology of dense granular suspensions, J. Fluid Mech. **852**, P1 (2018).
[10] E. C. Eckstein, D. G. Bailey, and A. H. Shapiro, Self-diffusion of particles in shear flow of a suspension, J. Fluid Mech. **79**, 191 (1977).
[11] D. Leighton and A. Acrivos, The shear-induced migration of particles in concentrated suspensions, J. Fluid Mech. **181**, 415 (1987).
[12] P. R. Nott and J. F. Brady, Pressure-driven flow of suspensions: Simulation and theory, J. Fluid Mech. **275**, 157 (1994).
[13] P. M. Kulkarni and J. F. Morris, Suspension properties at finite Reynolds number from simulated shear flow, Phys. Fluids **20**, 040602 (2008).
[14] P. R. Nott, E. Guazzelli, and O. Pouliquen, The suspension balance model revisited, Phys. Fluids **23**, 043304 (2011).
[15] M. Souzy, H. Lhuissier, E. Villermaux, and B. Metzger, Stretching and mixing in sheared particulate suspensions, J. Fluid Mech. **812**, 611 (2017).
[16] D. G. Wang, S. S. Sadhal, and C. S. Campbell, Particle rotation as a heat transfer mechanism, Int. J. Heat Mass Transf. **32**, 1413 (1989).
[17] A. S. Ahuja, Augmentation of heat transport in laminar flow of polystyrene suspensions. I. Experiments and results, J. Appl. Phys. **46**, 3408 (1975).
[18] A. S. Ahuja, Augmentation of heat transport in laminar flow of polystyrene suspensions. II. Analysis of the data, J. Appl. Phys. **46**, 3417 (1975).
[19] L. Leal, Macroscopic transport properties of a sheared suspension, J. Colloid Interface Sci. **58**, 296 (1977).
[20] Y. Chung and L. Leal, An experimental study of the effective thermal conductivity of a sheared suspension of rigid spheres, Int. J. Multiphase Flow **8**, 605 (1982).
[21] B. Metzger, O. Rahli, and X. Yin, Heat transfer across sheared suspensions: Role of the shear-induced diffusion, J. Fluid Mech. **724**, 527 (2013).
[22] A. Nir and A. Acrivos, The effective thermal conductivity of sheared suspensions, J. Fluid Mech. **78**, 33 (1976).
[23] A. Nadim, R. Cox, and H. Brenner, Taylor dispersion in concentrated suspensions of rotating cylinders, J. Fluid Mech. **164**, 185 (1986).
[24] C. W. Sohn and M. Chen, Microconvective thermal conductivity in disperse two-phase mixtures as observed in a low velocity Couette flow experiment, ASME J. Heat Transf. **103**, 47 (1981).
[25] S. Shin and S.-H. Lee, Thermal conductivity of suspensions in shear flow fields, Int. J. Heat Mass Transf. **43**, 4275 (2000).
[26] K. Yeo and M. R. Maxey, Dynamics and rheology of concentrated, finite-Reynolds-number suspensions in a homogeneous shear flow, Phys. Fluids **25**, 053303 (2013).
[27] F. Picano, W.-P. Breugem, D. Mitra, and L. Brandt, Shear thickening in non-Brownian suspensions: An excluded volume effect, Phys. Rev. Lett. **111**, 098302 (2013).
[28] G. Subramanian and D. L. Koch, Inertial effects on the transfer of heat or mass from neutrally buoyant spheres in a steady linear velocity field, Phys. Fluids **18**, 073302 (2006).
[29] A. P. Merin and V. Srinivasan, Heat transfer measurements in neutrally buoyant suspensions in the inertial regime, in *Proceedings of the ASME 2022 Heat Transfer Summer Conference collocated with the ASME 2022 16th International Conference on Energy Sustainability, Philadelphia, USA* (ASME, New York, 2022), p. V001T13A009.
[30] L. Wang, D. L. Koch, X. Yin, and C. Cohen, Hydrodynamic diffusion and mass transfer across a sheared suspension of neutrally buoyant spheres, Phys. Fluids **21**, 033303 (2009).
[31] M. N. Ardekani, O. Abouali, F. Picano, and L. Brandt, Heat transfer in laminar Couette flow laden with rigid spherical particles, J. Fluid Mech. **834**, 308 (2018).

[32] J.-P. Matas, J. F. Morris, and E. Guazzelli, Transition to turbulence in particulate pipe flow, Phys. Rev. Lett. **90**, 014501 (2003).
[33] P. Chossat and G. Iooss, Primary and secondary bifurcations in the Couette-Taylor problem, Jpn. J. Appl. Math. **2**, 37 (1985).
[34] D. Coles, Transition in circular Couette flow, J. Fluid Mech. **21**, 385 (1965).
[35] E. Linares-Guerrero, M. L. Hunt, and R. Zenit, Effects of inertia and turbulence on rheological measurements of neutrally buoyant suspensions, J. Fluid Mech. **811**, 525 (2017).
[36] Y. Song and M. Hunt, Rheological measurements and transition to turbulence for moderate Reynolds number inertial suspensions, J. Fluid Mech. **988**, A19 (2024).
[37] J. A. Balderas-López, A. Mandelis, and J. A. Garcia, Thermal-wave resonator cavity design and measurements of the thermal diffusivity of liquids, Rev. Sci. Instrum. **71**, 2933 (2000).
[38] W. E. Acree, Jr. and J. S. Chickos, Phase transition enthalpy measurements of organic and organometallic compounds, in *NIST Chemistry WebBook*, edited by P. J. Linstrom and W. G. Mallard, NIST Standard Reference Database Number 69 (National Institute of Standards and Technology, Gaithersburg, MD, 2026).
[39] N. Ravi, V. Gabeur, Y.-T. Hu, R. Hu, C. Ryali, T. Ma, H. Khedr, R. Rädle, C. Rolland, L. Gustafson, *et al.*, SAM 2: Segment anything in images and videos, in *International Conference on Learning Representations* (OpenReview.net, 2025), Vol. 2025, pp. 28085–28128.
[40] A. D. Brailsford and K. G. Major, The thermal conductivity of aggregates of several phases, including porous materials, Br. J. Appl. Phys. **15**, 313 (1964).
[41] A. Karnis, H. Goldsmith, and S. Mason, The kinetics of flowing dispersions: I. Concentrated suspensions of rigid particles, J. Colloid Interface Sci. **22**, 531 (1966).
[42] M. V. Majji and J. F. Morris, Inertial migration of particles in Taylor-Couette flows, Phys. Fluids **30**, 033303 (2018).
[43] M. V. Majji, S. Banerjee, and J. F. Morris, Inertial flow transitions of a suspension in Taylor–Couette geometry, J. Fluid Mech. **835**, 936 (2018).
[44] P. Ramesh, S. Bharadwaj, and M. Alam, Suspension Taylor–Couette flow: Co-existence of stationary and travelling waves, and the characteristics of Taylor vortices and spirals, J. Fluid Mech. **870**, 901 (2019).
[45] G. Segre and A. Silberberg, Behaviour of macroscopic rigid spheres in Poiseuille flow part 2. Experimental results and interpretation, J. Fluid Mech. **14**, 136 (1962).
[46] B. Ho and L. Leal, Inertial migration of rigid spheres in two-dimensional unidirectional flows, J. Fluid Mech. **65**, 365 (1974).
[47] J.-P. Matas, J. F. Morris, and É. Guazzelli, Inertial migration of rigid spherical particles in Poiseuille flow, J. Fluid Mech. **515**, 171 (2004).
[48] C. D. Andereck, S. Liu, and H. L. Swinney, Flow regimes in a circular Couette system with independently rotating cylinders, J. Fluid Mech. **164**, 155 (1986).
[49] M. Ghosh and M. Alam, Instabilities and particle-induced patterns in co-rotating suspension Taylor–Couette flow, J. Fluid Mech. **995**, R4 (2024).
[50] S. P. Singh, M. Ghosh, and M. Alam, Counter-rotating suspension Taylor–Couette flow: Pattern transition, flow multiplicity and the spectral evolution, J. Fluid Mech. **944**, A18 (2022).